

See discussions, stats, and author profiles for this publication at: <https://www.researchgate.net/publication/238036800>

# Flow past a circular cylinder at low Reynolds number: Oblique vortex shedding

Article in Physics of Fluids · May 2010

DOI: 10.1063/1.3410925

---

CITATIONS

22

READS

2,935

---

2 authors:



Suresh Behara

Aditya Institute of Technology & Management

12 PUBLICATIONS 262 CITATIONS

[SEE PROFILE](#)



Sanjay Mittal

Indian Institute of Technology Kanpur

171 PUBLICATIONS 6,345 CITATIONS

[SEE PROFILE](#)

Some of the authors of this publication are also working on these related projects:



VIV of Bluff bodies [View project](#)



Computation of flow in supersonic intakes and nozzles [View project](#)

# Flow past a circular cylinder at low Reynolds number: Oblique vortex shedding

Suresh Behara and Sanjay Mittal<sup>a)</sup>

*Department of Aerospace Engineering, Indian Institute of Technology Kanpur, Kanpur 208 016, India*

(Received 15 May 2009; accepted 29 March 2010; published online 4 May 2010)

Oblique shedding in the laminar regime for the flow past a nominally two-dimensional circular cylinder has been investigated numerically via a stabilized finite element method. No-slip condition on one of the sidewalls leads to the formation of a boundary layer which promotes oblique vortex shedding. Computations are carried out for three values of Reynolds number (Re): 60, 100, and 150. Cellular shedding is observed in all cases. Three cells are observed along the span for the Re=60 flow while only two cells are formed at Re=100 and 150. Spotlike vortex dislocations form at the junction of the cells. The frequency of the appearance of the dislocations increases with Re. Cellular shedding leads to low frequency modulation in the time histories of aerodynamic coefficients. Lowest value of drag is achieved at a time instant corresponding to the appearance of a new dislocation in the near wake. The vortex shedding frequency as well as the oblique angle of the primary vortices is found to vary with time for the Re=60 flow. Their variation is also related to the appearance of dislocations in the near wake. It is found that the vortex shedding frequency ( $St_\theta$ ) is related to the frequency observed for parallel shedding ( $St_0$ ) and the angle of the oblique vortices ( $\theta$ ) by the relation:  $St_\theta = St_0 \cos \theta$ . This relationship was proposed earlier for the case when the vortex shedding frequency and the oblique angle do not change with time. The velocity fluctuations are found to decrease with increase in  $\theta$ . For the Re=100 and 150 flow, the oblique angle of the vortices and the shedding frequency outside the end cell do not change with time. However,  $\theta$  and  $St_\theta$  depend on the aspect ratio of the cylinder. The oblique shedding angle, for various lengths of endplate and Re, is found to vary linearly with the thickness of the boundary layer on the side wall. © 2010 American Institute of Physics. [doi:10.1063/1.3410925]

## I. INTRODUCTION

Flow past bluff bodies have received continued research attention over several years because of its significance in engineering applications as well as rich flow physics. Despite its simple geometry, the flow past a nominally two-dimensional (2D) circular cylinder is associated with most of the aspects related to other bluff bodies with more complex geometries. A comprehensive description of the various regimes encountered in the flow past a circular cylinder has been given by Williamson<sup>1</sup> in a review article. The steady flow past a circular cylinder loses stability at  $Re \sim 47$  via the instability of the wake.<sup>2</sup> This instability leads to the von Karman vortex shedding. However, the flow still remains two-dimensional. At  $Re$  in the range of 180–190, the three-dimensional (3D) instabilities in the wake appear. Another interesting aspect related to the wake is the angle between the axis of the cylinder and that of the vortices being shed. This leads to oblique versus parallel modes of vortex shedding and is largely determined by the experimental conditions.

Several experimental studies in the past<sup>3–6</sup> have revealed that oblique shedding is a result of the end conditions in the wind/water tunnel. The end conditions affect the vortex shedding over the entire span of the cylinder even if the length of cylinder is very large compared with its diameter. They have

a direct effect over a region of the length that is  $10\text{--}20D$  from the end, where  $D$  is diameter of the cylinder. The effect on the remaining span is indirect. The disturbances related to the bending of vortices are passed on from one shed vortex to another over the span.<sup>5</sup> Therefore, the end conditions which promote oblique mode of shedding lead to vortices that are parallel in the initial transient period. This phenomenon was corroborated by Albarede and Monkewitz<sup>7</sup> via modeling the flow with the Ginzburg–Landau equations. It is possible to obtain parallel shedding by manipulating end conditions via end plates<sup>5</sup> or via other techniques, such as using control cylinders.<sup>8</sup>

Williamson<sup>9</sup> observed that in the laminar regime ( $49 \leq Re \leq 178$ ), two curves for Strouhal-Re exist. The lower curve, with a discontinuity at  $Re=64$ , is observed for oblique shedding. Parallel shedding, induced by manipulating end conditions, leads to the higher Strouhal-Re curve. In another experimental effort Williamson<sup>5</sup> established that the angle of the vortices with the spanwise axis of the cylinder modifies the vortex shedding frequency. He proposed a relation between the frequency of oblique shedding,  $f_\theta$ , and the oblique angle,  $\theta$ , as  $f_\theta = f_0 \cos \theta$ , where  $f_0$  is the frequency when parallel shedding takes place. It was noticed that the oblique angle increases with the increase in  $Re$  and experiences sudden rise at  $Re=64$ , which explains the discontinuity in the  $St_\theta$ -Re plot. As  $Re$  is increased up to 100,  $\theta$  decreases and thereafter, it remains almost constant.

<sup>a)</sup>Electronic mail: smittal@iitk.ac.in.

It has been observed in several experimental investigations that the end effects lead to spanwise variation of shedding frequency. For example, Gerich and Eckelmann<sup>10</sup> noticed that near the end of cylinder, ranging at 6–15 diameters along the span, the frequency of vortex shedding is 10%–15% less than the frequency in the central region. Cellular shedding and the related vortex dislocations have been studied by various researchers in the past.<sup>11–13</sup> Leweke *et al.*<sup>14</sup> proposed a mechanism for the formation of cells. They attributed it to the spatial growth of the secondary Eckhaus instability of oblique shedding when the shedding angle exceeds a certain critical value. This causes the vortex to break along the span and the resulting cells settle to a lower oblique shedding angle. The break region becomes the new end condition for the next cell. The perturbation at the new end grows leading to another break if the oblique angle is above the stability limit. The cell structure is, therefore, a consequence of the successive destabilization of the oblique shedding patterns.

Williamson<sup>5</sup> observed two kinds of oblique vortex shedding modes. For  $64 < \text{Re} < 178$ , the vortex shedding takes place in two cells. This is referred to as the periodic oblique shedding. The smaller cell that is closer to the end plates has a smaller shedding frequency, while a regular chevron shaped vortex pattern is observed in the middle cell with a single frequency. However, a different shedding pattern is observed for  $\text{Re} < 64$ . The flow is associated with three frequencies along the span. For each of the two halves of the span the vortex shedding frequency increases as one goes from the end-to-middle and then the central cell. This mode of shedding is referred to as the quasiperiodic oblique shedding.

Inoue and Sakuragi<sup>15</sup> carried out computations for a cylinder of finite span with free ends for  $40 \leq \text{Re} \leq 300$  and  $0.5 \leq L/D \leq 100$ , where  $L$  is the spanwise length of the cylinder. In a very comprehensive study, they observed a drastic change in the wake structure depending on the value of  $\text{Re}$  and  $L/D$ . Five basic patterns of vortex shedding were identified. They obtained periodic oblique vortex shedding at  $\text{Re}=150$ , for  $L/D=100$  and quasiperiodic shedding at  $\text{Re}=60$  with  $L/D=70$ . The length of the central cell in the periodic oblique shedding pattern was found to decrease with decrease in  $L/D$ . The length of the end cell ( $\sim 10D$ ), however, remains unchanged.

Except for the effort by Mittal<sup>16</sup> we are not aware of any other numerical effort where the oblique vortex shedding in a uniform flow has been investigated for a nominally 2D cylinder. Mittal<sup>16</sup> carried out a numerical study for a cylinder with aspect ratio 16 at  $\text{Re}=100$ , 300, and 1000. The end conditions are specified to model the effect of a wall. The flow for  $\text{Re}=100$  was found to be very organized, devoid of any vortex dislocations and was associated with only one cell along the cylinder span. The flow at  $\text{Re}=1000$  was interspersed with vortex dislocations and the vortex shedding angle varied, both, temporally and along the span. It was concluded that the wake transition regime, that is known to occur in the  $\text{Re}$  range of 190–250 for large aspect-ratio cylinders, is either extended and/or delayed for a cylinder of small aspect ratio with “no-slip” walls.

In the present effort we utilize a stabilized finite element method to compute flow past a circular cylinder in the presence of a no-slip wall at one of the ends of the cylinder. Unlike slip walls that lead to parallel shedding, this end condition is expected to produce oblique vortex shedding. The aspect ratio of the cylinder is 60. To save on computational cost only one half of the span of the cylinder is considered: symmetry conditions are imposed on the other wall. Computations are carried out for three values of Reynolds number: 60, 100 and 150. These Reynolds numbers are low enough so that the flow is devoid of the complexities associated with 3D instabilities in the wake, such as mode A and mode B, which are associated with flows at  $\text{Re}$  larger than 190, approximately. The numerical method is identical to the one used in our earlier work.<sup>16</sup> The simulations are utilized to study the frequency of vortex dislocations and its variation with  $\text{Re}$ . The relation between the frequency of dislocations, time variation of angle of oblique vortices and the aerodynamic coefficients is investigated. It is found that the frequency of appearance of the dislocations is related to the frequency of the time variation of the angle of the oblique vortices. It is also noticed that the dislocations in the near wake lead to low frequency modulation in the amplitude of aerodynamic coefficients in their time traces.

The outline of this paper is as follows. Section II describes the governing equations, problem setup, finite element mesh, boundary conditions, and other computational details. The main results and their discussion are presented in Sec. III and we end with concluding remarks in Sec. IV.

## II. GOVERNING EQUATIONS AND COMPUTATIONAL DETAILS

### A. The Navier–Stokes equations

Let  $\Omega \subset \mathfrak{R}^{n_{sd}}$  and  $(0, T)$  be the spatial and temporal domains, respectively, where  $n_{sd}$  is the number of space dimensions, and let  $\Gamma$  denote the boundary of  $\Omega$ . The spatial and temporal coordinates are denoted by  $\mathbf{x}$  and  $t$ . The Navier–Stokes equations governing incompressible fluid flow are

$$\rho \left( \frac{\partial \mathbf{u}}{\partial t} + \mathbf{u} \cdot \nabla \mathbf{u} - \mathbf{f} \right) - \nabla \cdot \boldsymbol{\sigma} = \mathbf{0} \quad \text{on } \Omega \times (0, T), \quad (1)$$

$$\nabla \cdot \mathbf{u} = 0 \quad \text{on } \Omega \times (0, T). \quad (2)$$

Here  $\rho$ ,  $\mathbf{u}$ ,  $\mathbf{f}$ , and  $\boldsymbol{\sigma}$  are the density, velocity, body force, and the stress tensor, respectively. The stress tensor is written as the sum of its isotropic and deviatoric parts

$$\boldsymbol{\sigma} = -p\mathbf{I} + \mathbf{T}, \quad \mathbf{T} = 2\mu\boldsymbol{\varepsilon}(\mathbf{u}), \quad \boldsymbol{\varepsilon}(\mathbf{u}) = \frac{1}{2}[(\nabla \mathbf{u}) + (\nabla \mathbf{u})^T], \quad (3)$$

where  $p$ ,  $\mathbf{I}$ , and  $\mu$  are the pressure, identity tensor, and dynamic viscosity, respectively. Both the Dirichlet and Neumann-type boundary conditions are accounted for, and represented as

$$\mathbf{u} = \mathbf{g} \quad \text{on } \Gamma_g, \quad \mathbf{n} \cdot \boldsymbol{\sigma} = \mathbf{h} \quad \text{on } (\Gamma)_h, \quad (4)$$

where  $\Gamma_g$  and  $\Gamma_h$  are complementary subsets of the boundary  $\Gamma$  and  $\mathbf{n}$  is its unit normal vector. The details of the boundary

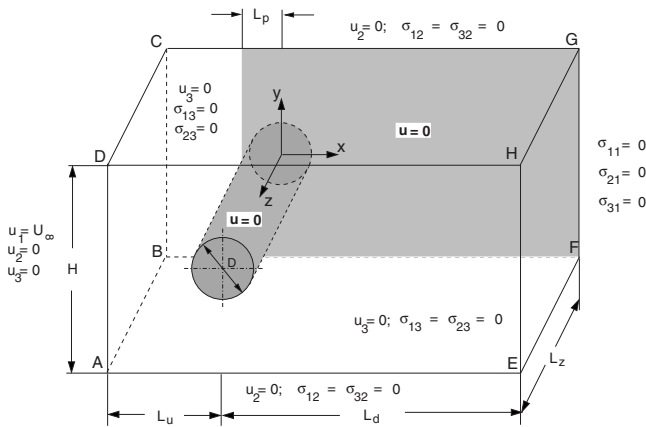


FIG. 1. Flow past a cylinder: schematic of the computational domain and the boundary conditions.

conditions for the present problem are shown in Fig. 1 and described in Sec. III. The initial condition on the velocity is specified on  $\Omega$  at  $t=0$

$$\mathbf{u}(\mathbf{x}, 0) = \mathbf{u}_0 \quad \text{on} \quad \Omega, \quad (5)$$

where  $\mathbf{u}_0$  is divergence-free.

The coefficient of aerodynamic force  $C_x$  is calculated by integrating the pressure and viscous stresses around the surface of the cylinder. For a cylinder whose axis is normal to the flow its three components are as follows:  $C_L$ , the lift coefficient that is normal to the flow direction and cylinder span,  $C_D$ , the drag coefficient that is along the flow direction, and  $C_S$ , the side force coefficient, that acts along the spanwise direction.  $C_x$  is given as

$$C_x = \frac{1}{\frac{1}{2}\rho U_\infty^2 LD} \int_{\Gamma_{cyl}} \boldsymbol{\sigma} \cdot \mathbf{n} d\Gamma, \quad (6)$$

where  $\Gamma_{cyl}$  is the boundary of the cylinder and  $L$  is the spanwise length of the cylinder.

The governing equations are discretized using the stabilized finite element formulation and the resulting equation system is solved using the Generalized Minimal RESidual (GMRES) technique<sup>17</sup> in conjunction with diagonal preconditioners. The details of the formulation used in the present work can be found in the article by Mittal.<sup>16</sup>

## B. Finite element mesh and boundary conditions

Figure 1 shows the schematic of the computational domain and boundary conditions employed. A cylinder of unit radius occupies the entire span,  $L_z$ , of the domain. Free-stream flow is along the  $x$ -axis on the upstream face ABCD, while the axis of the cylinder is along the  $z$ -axis. The upstream and downstream boundaries are located at a distance of  $L_u$  and  $L_d$ , respectively, from the center of the cylinder.  $H$  is the height of the domain.

On the upstream face, ABCD in Fig. 1, uniform flow is prescribed. At the outflow boundary, EFGH, the stress vector

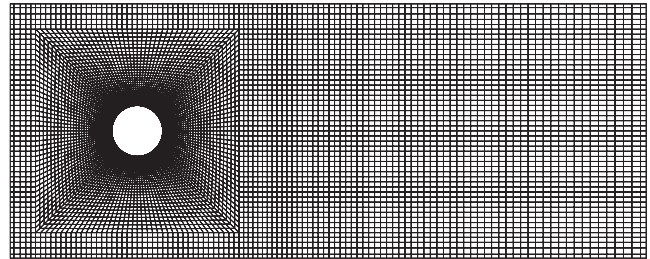


FIG. 2. Flow past a cylinder: close-up view of the 2D section of the finite element mesh in the  $x$ - $y$  plane. The 3D mesh consists of 4 171 300 nodes and 4 080 000 eight-noded hexahedral elements.

is set to zero. No-slip condition on the velocity is specified on the cylinder surface as well as the side wall BFGC for  $x \geq -L_p$ . Symmetry condition is used on all other walls of the computational domain, i.e., the velocity component normal to that wall and the stress vector components in the plane of the wall are assigned zero values. Boundary layer develops on the side wall BFGC following the specification of no-slip condition on velocity and promotes oblique vortex shedding. The computations have been carried out with  $L_u=50D$ ,  $L_d=125D$ ,  $L_z=30D$ ,  $L_p=5D$ , and  $H=100D$ . Symmetry conditions on the side wall, ADHE, allows one to simulate only one half of the cylinder span. Therefore, in the present work even though  $L_z$  is  $30D$ , the effective aspect ratio of the cylinder is  $AR=60$ . The effect of the location of the upstream, downstream and lateral boundaries has been studied in detail in an earlier work by Prasanth and Mittal<sup>18</sup> for 2D computations past a freely vibrating cylinder. It was found that  $L_u=15D$ ,  $L_d=25.5D$ , and  $H=40D$  are adequate to give sufficiently accurate results. The effect of  $L_p$  is reported later in the paper.

The Reynolds number,  $Re$ , is based on the diameter of the cylinder, free-stream speed,  $U_\infty$ , and kinematic viscosity of the fluid,  $\nu$ . The finite element mesh consists of 4 171 300 nodes and 4 080 000 eight-noded hexahedral elements. A close-up view of the 2D section of the mesh, in the  $xy$  plane, is shown in Fig. 2. The 3D mesh is obtained by stacking 100 slices of the 2D mesh along span. The mesh, close to the cylinder surface, consists of 160 elements in the circumferential direction. The radial height of the first element on the cylinder surface is  $0.0005D$ . The distribution of mesh points along the span is nonuniform. More points are clustered near the wall with no-slip boundary condition to resolve the boundary layer. The height, along the span, of the first element on the surface of this wall is  $0.005D$ .

## C. Computational details

All the computations reported in this article have been carried out on a 64 processor Linux cluster at IIT Kanpur. It is a 32 node parallel computing machine loaded with Message Passing Interface (MPI) libraries. Each node is equipped with two Intel Xeon processors with clock speed of 3.06 GHz. Each processing unit consists of a main memory unit of 2 Gbyte random access memory and 512 Kbyte L2 cache. The nodes communicate via a 1 Gbps network. All computations are carried out in 64 bit precision. Equal-in-

TABLE I.  $Re=150$ ,  $AR=60$  flow past a cylinder: details of the finite element meshes used and aerodynamic coefficients computed.  $S_e$  and  $S_L$  are the nondimensional vortex shedding frequency in the end and central cells, and  $\bar{C}_D$  and  $C_{L,\text{rms}}$  are the time-averaged drag- and rms value of the lift-coefficients, respectively.

Mesh	Nodes	Elements	$S_e$	$S_L$	$\bar{C}_D$	$C_{L,\text{rms}}$
<i>M1</i>	4 171 300	4 080 000	0.1514	0.1770	1.270	0.0647
<i>M2</i>	8 422 780	8 280 000	0.1536	0.1728	1.268	0.0655

order trilinear basis functions for velocity and pressure (eight-noded hexahedral element) are used and an eight point quadrature is employed for numerical integration. The equation systems resulting from the finite-element discretization of the flow equations are solved using the matrix-free implementation of the GMRES technique<sup>17</sup> in conjunction with diagonal preconditioners. A time step of  $\Delta t=0.10$  is used for all the computations. Three nonlinear iterations are carried out at each time step, and the size of the Krylov subspace is 20 with no restarts. 16 381 741 nonlinear coupled equations are solved at each time step. The solution to such large scale problems is made possible by the matrix-free implementation of the iterative solver that is fairly soft on the memory requirements associated with implicit methods. On ten processors of the Linux cluster, these computations require approximately 320 s/time step.

#### D. Convergence: Effect of spatial resolution

The adequacy of the spatial resolution of the finite element mesh employed for the computations reported in this paper is investigated. Two finite element meshes are used to compute the  $Re=150$  flow past a cylinder with  $AR=60$ . The boundary conditions are same as described in Sec. II B and shown in Fig. 1. The number of nodes and elements in each mesh is listed in Table I. In the  $x$ - $y$  plane, each 2D section of mesh *M1* consists of 41 300 nodes and 40 800 rectangular elements. These numbers for mesh *M2* are 55 780 and 55 200, respectively. The height of the layer of elements, along the span of the cylinder, lying on the no-slip side wall is  $0.0005D$  for mesh *M1*. The height of the elements that lie on the cylinder, normal to its surface, is  $0.005D$ . For the mesh *M2*, they are half these values. The element heights on the surface of cylinder and the no-slip side wall, are  $0.0025D$  and  $0.00025D$ , respectively, for mesh *M2*. The spatial extent of the computational domain for the two meshes is identical. The number of elements along the span of the cylinder for mesh *M1* and *M2* are 100 and 150, respectively. The time histories of the aerodynamic coefficients and the cross-flow component of velocity sampled at two probe locations are compared for the two meshes. The  $x/D$  and  $y/D$  coordinates for both the probes are 1.5 and 0.3, respectively. The spanwise location of the two probes is  $z/D=6.9$  and 15.1. These probes allow us to calculate the nondimensional vortex shedding frequency in the end and central cells:  $S_e$  and  $S_L$ . Table I shows the results from the two meshes. Excellent agreement in the values obtained from the two meshes demonstrates the adequacy of mesh *M1*.

### III. RESULTS

#### A. Overview

Computations are reported for three values of  $Re$ : 60, 100, and 150. Oblique mode of vortex shedding is observed in all the three cases. The no-slip condition at one of the side walls, in the present computations, promotes oblique vortex shedding. Figure 3 shows the instantaneous picture of the spanwise component of vorticity in the  $xz$  plane passing through the axis of the cylinder for  $Re=60$  and 150 for the fully evolved unsteady flow. Three cells along the span of the cylinder are observed for  $Re=60$ . As per the nomenclature in the literature,<sup>5</sup> we refer to these as end, middle, and central cells. For the  $Re=100$  and 150 only two cells are observed: end and central. Spotlike vortex dislocations mark the boundaries of the cells. The angle of the axes of the vortices, to the axis of the cylinder, is also different across the cell boundaries. Figure 4 shows the unsteady flow at  $Re=100$  for two values of  $L/D$ . The flow is very similar to that at  $Re=150$ . As expected, the aspect ratio of the cylinder has no significant effect on the structure of the flow except for the oblique shedding angle which is different for the two cases. The end cell region of the flow appears to be largely unaffected by the aspect ratio of the cylinder. This is consistent with the observation of Inoue and Sakuragi<sup>15</sup> that the length

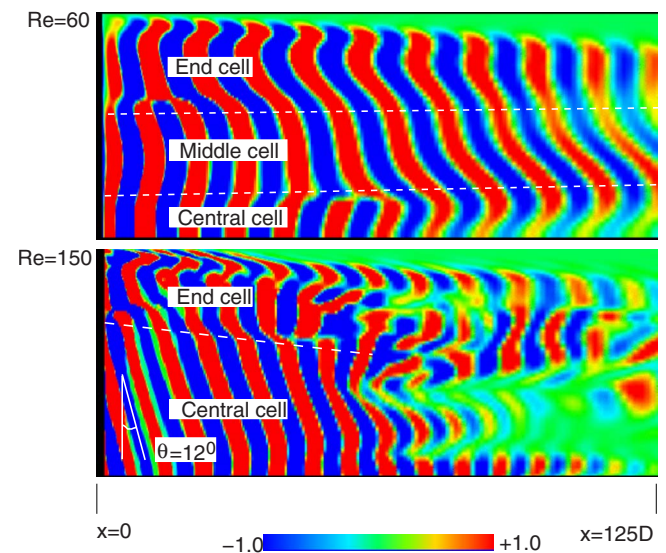


FIG. 3. (Color online) Flow past a circular cylinder: instantaneous picture of the spanwise component of vorticity in the  $xz$  plane passing through the axis of the cylinder for  $Re=60$  (top) and  $Re=150$  (bottom).

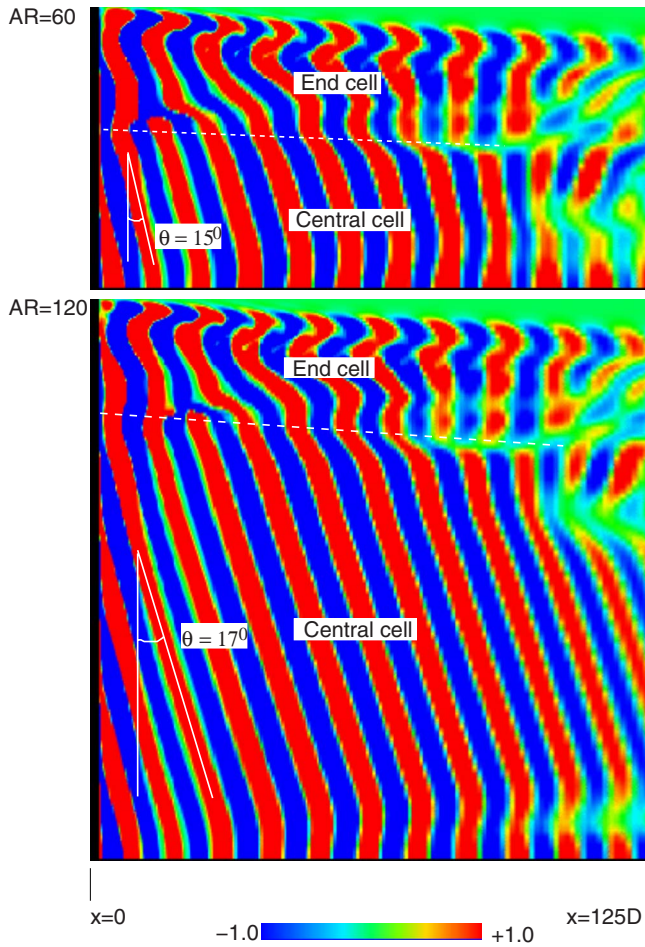


FIG. 4. (Color online)  $Re=100$  flow past a circular cylinder: instantaneous picture of the spanwise component of vorticity in the  $xz$  plane passing through the axis of the cylinder for (a)  $AR=60$  and (b)  $AR=120$ .

of the end cell does not change with  $L/D$ . The chevron-shaped pattern is more striking in the flow past cylinder with larger aspect ratio. It is found that the oblique shedding angle remains constant with time for the  $Re=100$  and 150 flow. However, it varies with time for the  $Re=60$  flow.

## B. Vortex shedding frequency

Figure 5 shows the time histories of the cross-flow component of velocity at three spanwise locations in the near wake of the cylinder and their frequency spectra. The first probe,  $P_1$ , reports data for the end cell. The frequency recorded by the second probe,  $P_2$ , represents the primary shedding frequency. It is located in the central cell for  $Re=100$  and 150 and in the middle cell for  $Re=60$ . The third probe,  $P_3$ , records the data in the central cell for all the  $Re$  considered. The vortex shedding frequency in each cell is found to vary with time for the  $Re=60$  flow. The Strouhal numbers corresponding to the peaks  $f_e$ ,  $f_m$ , and  $f_c$ , as shown in Fig. 5(a) are 0.1238, 0.1309, and 0.1345, respectively. The corresponding values reported by Williamson<sup>5</sup> for oblique shedding at  $Re=59.7$  for a cylinder with  $AR=90$  are  $S_e=0.1155$ ,  $S_L=0.1282$ , and  $S_U=0.1323$ . There is good agreement in the values for the middle and central cells. However, there is a difference in the values for the end cell from the present

computations and experiments by Williamson.<sup>5</sup> It is shown later in the paper that the shedding frequency within the end cell, for  $Re=60$ , varies between 0.11 and 0.13. The values reported by Williamson<sup>5</sup> as well as the dominant frequency from the present computations fall within this range. It is also possible that the difference in the end conditions in the experiments by Williamson<sup>5</sup> and the present study might contribute to the difference in  $S_e$  for the two studies.

Computations for the  $Re=100$  flow with  $AR=60$  result in  $St=0.1416$  and 0.1587 for the end and central cells, respectively. These numbers are in very good agreement with those reported by Williamson<sup>5</sup> for the  $Re=99.6$  flow:  $S_e=0.1407$  and  $S_L=0.1602$ . The oblique angle of the vortices in the  $Re=100$  flow, as shown in Fig. 3, is found to be  $\theta=15^\circ$ . Computations have also been carried out for  $AR=120$ . The vortex shedding frequency and oblique angle of the vortices for this case are found to be  $St_\theta=0.1596$  and  $\theta=17^\circ$ . Williamson,<sup>5</sup> for  $AR=90$ , reported  $St_\theta=0.1602$  and  $\theta=12.46^\circ$ . Using the relationship  $St_0=St_\theta/\cos(\theta)$ , he calculated the non dimensional frequency for parallel vortex shedding to be  $St_0=0.1641$ . The corresponding values from the present computations are  $St_0=0.1632$  for  $AR=60$  and 0.1668 for  $AR=120$ . The  $St_0$  value from the two sets of computations are virtually identical and in excellent agreement with those reported by Williamson.<sup>5</sup> We observe that the oblique shedding angle, as well as the vortex shedding frequency, is different for the two computations with different  $AR$ . This observation is also in line with that of Williamson;<sup>5</sup> he reported different values of  $St$  for models with different  $AR$ . For  $Re=150$  the Strouhal number corresponding to the vortex shedding frequency is found to be  $St_\theta=0.177$ . The oblique shedding angle is measured to be  $\theta=12^\circ$ , which results in  $St_0=0.1809$ . The values reported by Williamson<sup>5</sup> for the model with  $AR=90$  are  $St=0.1788$ ,  $\theta=12.82^\circ$ , and  $St_0=0.1834$ . Zhang *et al.*<sup>19</sup> carried out computations with slip walls and observed  $St_0 \sim 0.19$ .

## C. Vortex dislocations

### 1. $Re=60$ flow

Figure 5(a) shows the time variation of the cross-flow component of velocity and its frequency spectra in each of the three cells. The vortex shedding in the three cells takes place at different frequencies. The dominant frequency in the end, middle, and central cells is marked as  $f_e$ ,  $f_m$ , and  $f_c$ , respectively. The shedding frequency increases from the end cell toward the central cell. Vortex dislocations occur at the boundaries between the cells. These dislocations occur periodically in time. Figure 6 shows spanwise component of vorticity in the  $xz$  plane passing through the axis of the cylinder at various time instants for the fully evolved unsteady flow. The time evolution of the vortices as well as the spotlike dislocations, marked as  $D1$  and  $D2$  can be observed in the figure. The frequency of the appearance of  $D1$ , the dislocation at the junction of middle and end cells, is given by  $f_m-f_e$ . Similarly, the dislocation  $D2$ , at the junction of middle and central cells, appear at a frequency of  $f_c-f_m$ . The frequency of the appearance of the dislocations can also be observed visually from Fig. 6.

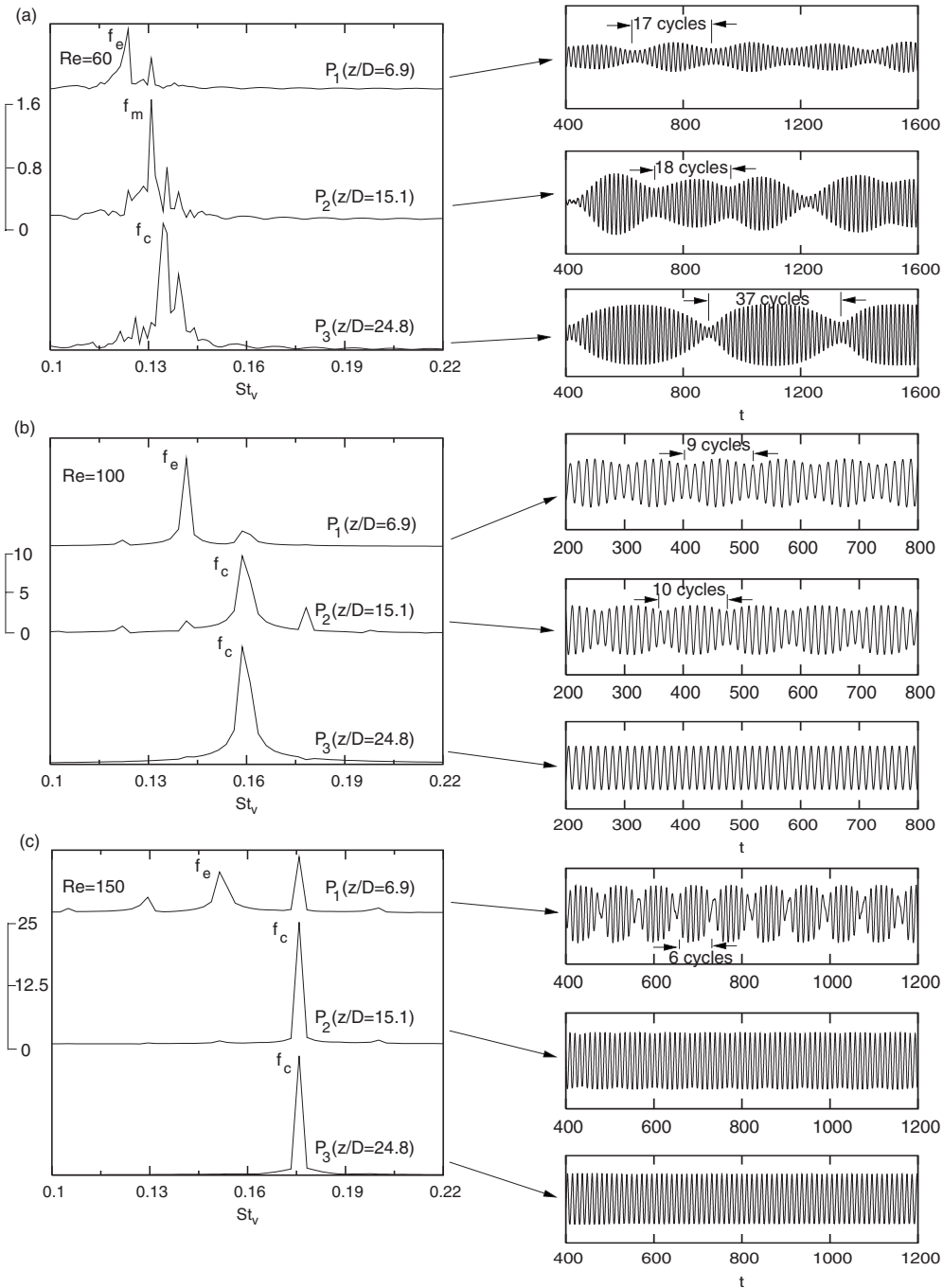


FIG. 5. Flow past a circular cylinder: time histories of the cross-flow component of velocity,  $v$  and their power spectra at three probe locations at various  $Re$ . The  $(x/D, y/D)$  location for all the three probes is  $(1.5, 0.3)$ .

The cellular structure of shedding with different frequencies leads to the beating phenomenon as can be observed from the time histories shown in Fig. 5(a). Beats have been observed in other flow situations as well. For example, Inoue and Suzuki<sup>20</sup> studied the sound generated by placing three square cylinders in uniform flow at low Mach number. They observed beats in the sound which are the result of two different Strouhal frequencies. The shedding from the two end cylinders occurs at the same frequency, while, a slightly higher frequency is observed from the cylinder at the center. It is seen in Fig. 6 that the dislocation  $D1$  forms at  $t=950$  in the very near wake and is referred to as  $D1_1$ . Another dislo-

cation, referred to as  $D1_2$ , appears at the same location at  $t = 1220$ . During this time  $D1_1$  is connected to a downstream location in the wake. A similar phenomenon is observed for the dislocation  $D2$ , albeit with a larger time period. The time period of the formation of dislocations is  $\sim 270$  time units for  $D1$  while it is  $\sim 440$  time units for  $D2$ . Another interesting observation that can be made from Fig. 6 is that the oblique angles of the vortices change with time. Later in the paper, we will show that this is related to the time variation in frequency of vortex shedding. This is also seen from the power spectra in Fig. 5(a) that shows a rather broad band behavior as opposed to a sharp peak.

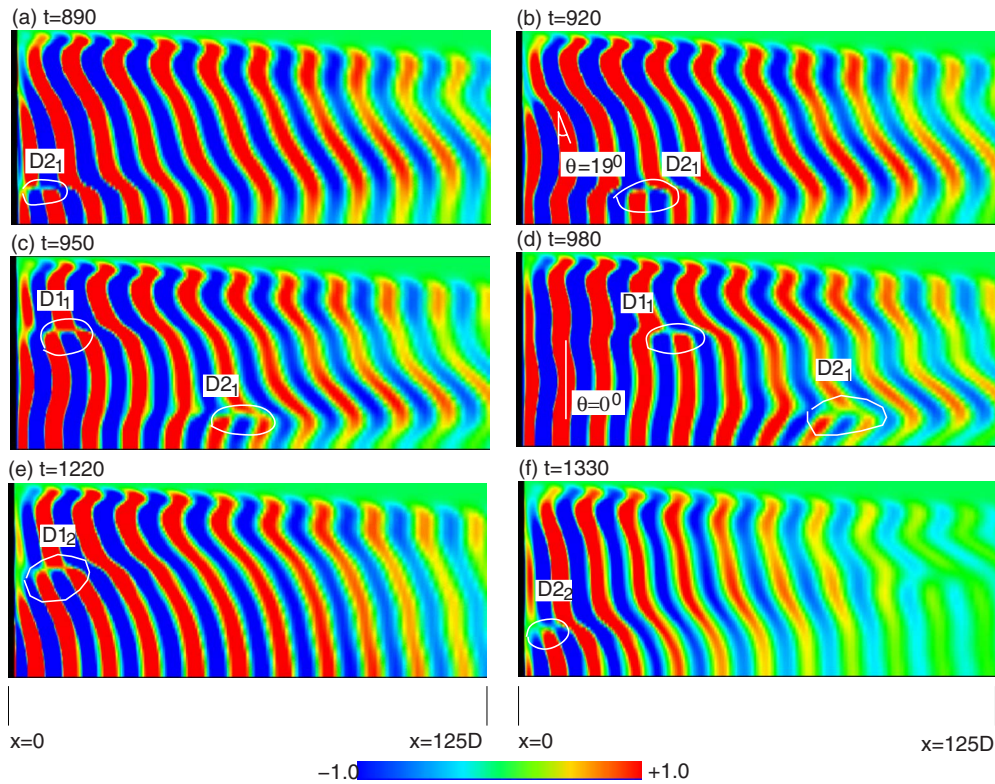


FIG. 6. (Color online)  $Re=60$  flow past a circular cylinder: spanwise component of vorticity in the  $xz$  plane passing through the axis of the cylinder at various time instants during one cycle of appearance of dislocation close to the slip wall.

Williamson<sup>5</sup> proposed a formula to find out the number of shedding cycles between the appearances of two consecutive dislocations. The number of vortex shedding cycles on the high frequency side of dislocation is given as  $n_U = S_U/(S_U - S_L)$ , where  $S_U$  and  $S_L$  are Strouhal numbers associated with the vortex shedding frequency in the cells at high and low frequency sides, respectively. The number of shedding cycles on the low frequency side of dislocation is given by  $n_L = n_U - 1$ . In the present simulations, at the junction of the end and middle cells, the values of  $S_L$  and  $S_U$  are the ones indicated by the peaks corresponding to  $f_e$  and  $f_m$  shown in Fig. 5(a). This, along with the formula proposed for  $n_U$  and  $n_L$ , results in 18 vortex shedding cycles during each low frequency cycle of the appearance of dislocations in the middle cell and 17 cycles in the end cell. These numbers are in excellent agreement with the actual number of cycles observed in the beating cycles from the present computations as marked in Fig. 5(a). Similarly, 37 cycles of vortex shedding are observed in the central cell during one cycle of appearance of dislocation  $D_2$ .

## 2. Re=100 and 150 flow

The flow pattern in the wake is very similar for the  $Re = 100$  and  $150$  flow. Only two cells along the span of the cylinder are observed: end and central cell. This is also seen from the time histories of the cross-flow component of velocity at three locations shown in Fig. 5. Unlike at  $Re=60$ , probes  $P_2$  and  $P_3$  show identical value of the dominant frequency. Only two vortex shedding frequencies exist along the span. Therefore, only one spotlike dislocation, at the

junction of end and central cells, arises in the flow. Figure 7 shows the spanwise component of vorticity in the  $xz$  plane passing through the axis of the cylinder for the fully evolved unsteady flow at various time instants during one cycle of the appearance of the spotlike dislocation. As the dislocation,  $D_1$ , moves downstream it evolves into a more complex flow structure formed out of a trail of dislocated vortex cells of small size marked as  $DT$  in the figures. The time histories for the various probes in Fig. 5 show that while the end cells undergo low frequency modulation, the time variation in the central cells is at almost constant amplitude. The frequency spectra of these signals show fairly sharp peaks. This is in contrast to the observation for the  $Re=60$  flow. Also, in the near wake, the vortex shedding angle in the central cell, which is seen to vary with time for  $Re=60$  in Fig. 6, is constant with time for the  $Re=100$  and  $150$  flow as seen from Fig. 7.

The formula proposed by Williamson<sup>5</sup> to find the number of shedding cycles between two consecutive appearances of a dislocation is applied to the  $Re=100$  and  $150$  flows. Excellent agreement is seen between the estimates from the formula and the results from the present numerical simulations. Figure 5(b) shows that 9 and 10 vortex shedding cycles occur in the low and high frequency sides of the dislocation, respectively, between two consecutive appearances of a dislocation at  $Re=100$ . For the  $Re=150$  flow, as seen in Fig. 5(c), 7 and 8 vortex shedding cycles are observed, respectively, on the low and high frequency sides of the dislocation. Figure 8 shows the variation of the frequency of dislocation with  $Re$ . For the  $Re=60$  flow, the dislocation close to the

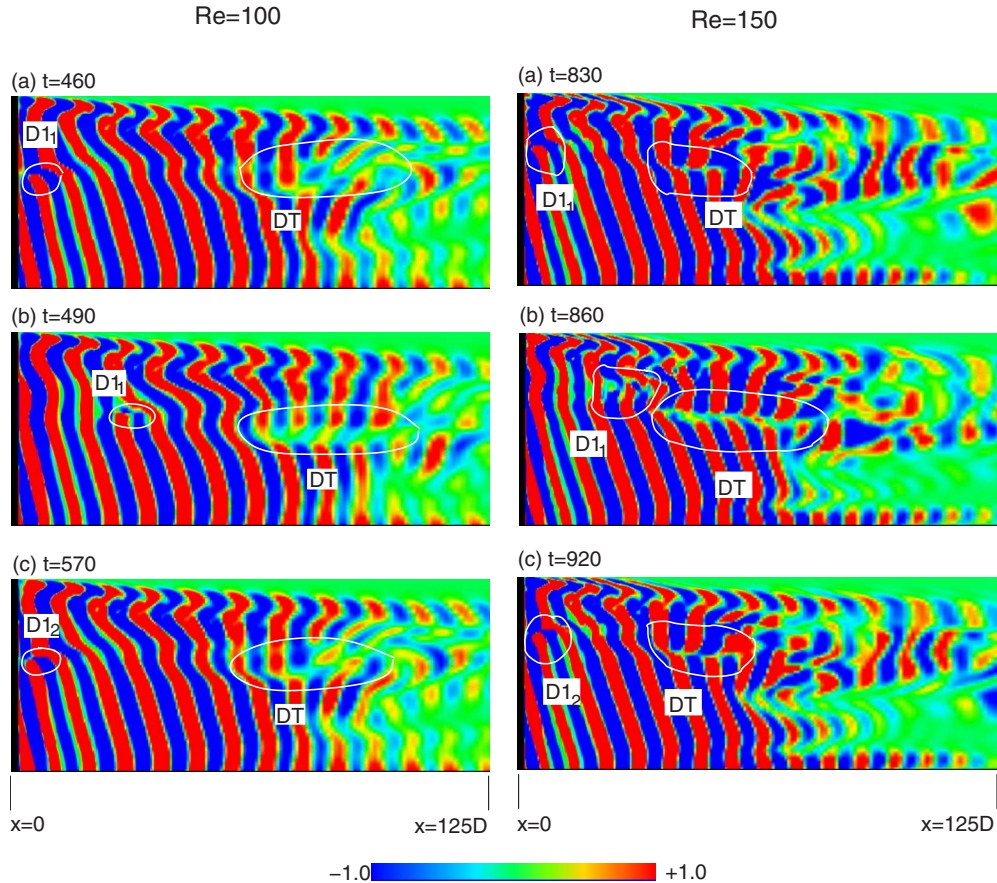


FIG. 7. (Color online) Flow past a circular cylinder: spanwise component of vorticity in the  $xz$  plane passing through the axis of the cylinder at various time instants during one cycle of appearance of dislocation.

no-slip wall is considered. It is observed that the dislocations appear more frequently as  $Re$  increases. However, the rate of increase in frequency decreases with the increase in  $Re$ .

#### D. Time variation of shedding frequency and oblique angle

The time variation of the cross-flow component of velocity at three spanwise locations is shown in Fig. 5. This data is utilized to study the time variation of the frequency of these signals. The time period of each cycle is found and

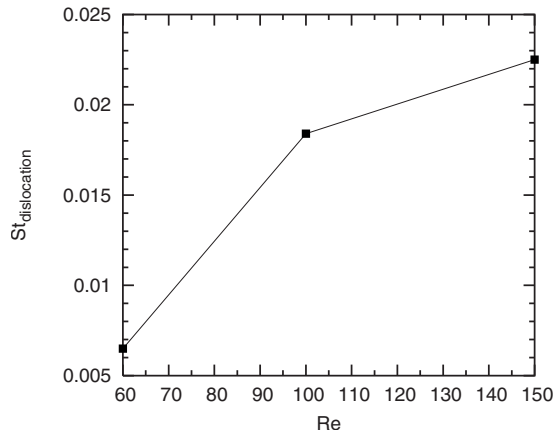


FIG. 8. Flow past a circular cylinder: variation of the frequency of appearance of vortex dislocation with  $Re$ .

used to estimate the instantaneous frequency. The time histories of the Strouhal number corresponding to the instantaneous frequency are shown in Fig. 9. For  $Re=100$  and 150 the frequency is almost constant in the central cell. However, for the  $Re=60$  flow it is seen to vary with time for, both, the middle and central cells. The shedding frequency of the end cell undergoes modulation in the flow at all the three Reynolds numbers. The results from the present computations are consistent with the observations from laboratory experiments by Williamson.<sup>5</sup> The signal with the end cell is influenced by the middle and central cells. This is observed via the peaks in the power spectra of the signal in the end-cell that correspond to shedding frequency in the middle and central cells. The fluid dynamic cause of these modulations remains an open question. Perhaps, they are a consequence of the interaction of the boundary layer on the side wall with the vortex shedding frequency as well as the angle of oblique vortices. The number of vortex shedding cycles in each low frequency cycle of the end cell is marked in Fig. 9. On comparing this to the time histories in Fig. 5, we observe that the frequency of the variation of  $St_v$  matches that of the appearance of spotlike vortex dislocations. Computations have also been carried out for the  $Re=150$  flow with slip boundary conditions on both the side walls of the domain. In such a scenario the flow is observed to be strictly 2D. It is devoid of dislocations and the time histories as well as the vortex shedding frequency do not exhibit any low frequency modula-

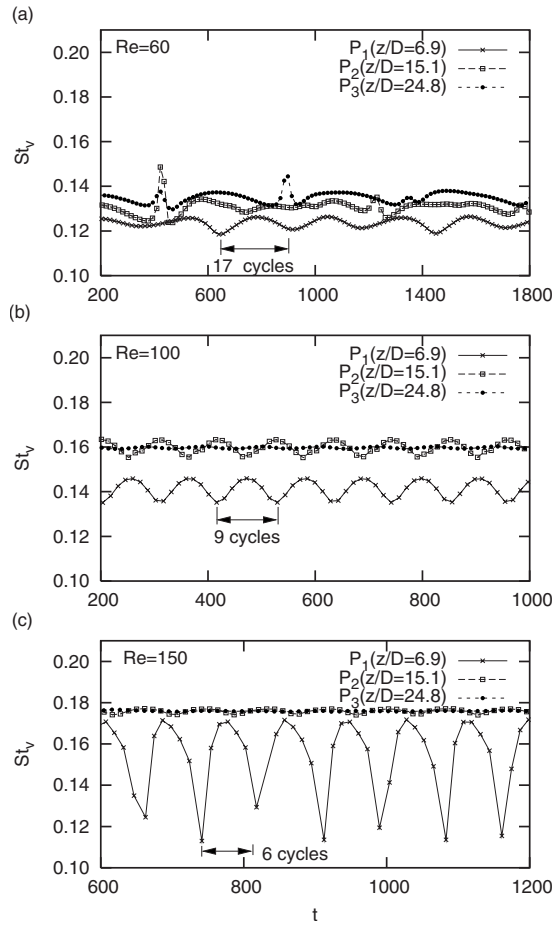


FIG. 9. Flow past a circular cylinder at various  $Re$ : variation of the Strouhal number  $St_v$  corresponding to the frequency of each cycle of  $v$  shown in Fig. 5.

tions. This shows that the low frequency modulation of the Strouhal frequency is related to the appearance of vortex dislocations which in turn are caused by the interaction of the boundary layer on the side wall with the primary vortices.

It is observed from Fig. 9 that the amplitude of variation of  $St_v$  of the end cells increases with  $Re$ . Najjar and Balachandar,<sup>21</sup> in their investigation of flow normal to a flat plate, found low frequency unsteadiness with a period of

approximately ten times the primary shedding period. They conjectured that the formation of streamwise and spanwise vortices is not in perfect synchronization and leads to the observed low frequency unsteadiness. They suggested an inverse relation between the spanwise coherence of the shed Karman vortices and the shedding period. It was pointed out that the higher circulation in the shed vortices results in higher mutual induction. Consequently, induced velocities are higher in the near wake which reduces the shedding period. Thus, Strouhal frequency increases with the increase in strength of the vortices. The observation from the present simulations that the beating frequency, corresponding to the appearance of successive dislocations, increases with  $Re$  is consistent with their suggestion. It is also noticed from the present computations that the minimum value of  $St_v$  occurs at a time instant corresponding to the appearance of spotlike dislocation in the near wake. For example, for the  $Re=150$  flow, Fig. 7 shows the appearance of the dislocation at  $t \sim 830$  and 920. The minimum value of  $St_v$  is also seen to occur at the same time instants [Fig. 9(c)]. This suggests that the spanwise loss of coherence in the vortex shedding is responsible for the lower Strouhal frequency.

The vortex shedding frequency in the central cell at  $Re = 100$  and 150 is almost constant with time and so is the angle of oblique vortices. For the  $Re=60$  flow, both the vortex shedding angle and the shedding frequency are found to vary with time in the middle and central cells. This raises an obvious question: is there a connection between the shedding frequency and the angle of oblique vortices? We attempt to address this issue. Williamson<sup>5</sup> proposed a relationship between the Strouhal numbers in the oblique shedding to the angle of the oblique vortices to the longitudinal axis of the cylinder as  $St_0 = St_\theta / \cos \theta$  where,  $St_0$  is the Strouhal number for parallel vortex shedding. Williamson<sup>5</sup> used this formula to collapse all the observed data onto a single  $St$ - $Re$  curve. To the best of our knowledge this formula has only been applied to the data when both  $St$  and  $\theta$  are constant with time. We investigate the application of this relationship to the  $Re=60$  flow, where both  $St_\theta$  and  $\theta$  show time variation.

The data for a time period spanning 800–1200 time units is considered for the analysis. The angle of the oblique vortices to the axis of the cylinder is measured at several time

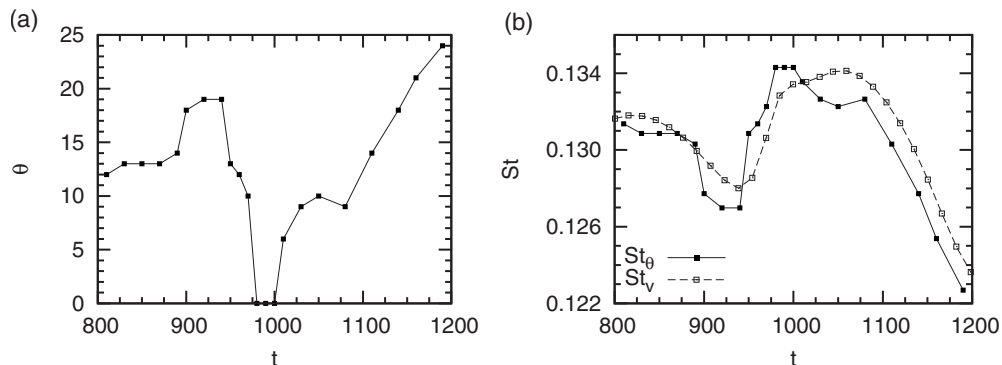


FIG. 10.  $Re=60$  flow past a circular cylinder: time histories of the (a) angle of the oblique vortices to the axis of the cylinder and (b) vortex shedding frequency corresponding to the frequency variation of the cross-flow component of velocity at a point in the middle cell located at  $(x/D=4.8, y/D=1.5,$  and  $z/D=15.1)$ . Also shown is the variation of  $St_\theta = St_0 \cos \theta$  by using the value of  $St_0$  for parallel shedding and  $\theta$  from (a).

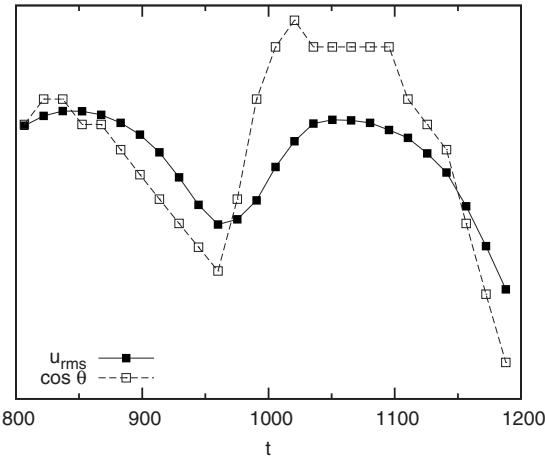


FIG. 11.  $Re=60$  flow past a circular cylinder: variation of the rms value of the streamwise component of velocity with time measured at  $(x/D, y/D, z/D) = (4.5, 0.3, 24.8)$ . Also shown is the time history of  $\cos \theta$ .  $\theta$  is the angle of primary vortices to the axis of the cylinder. The two signals are suitably scaled to bring out the phase between them.

instants from the plot of spanwise component of vorticity in the  $xz$  plane as shown in some of the frames of Fig. 6. The time variation of  $\theta$  is shown in Fig. 10(a). Shown in Fig. 10(b) is the variation of  $St_v$ , which is estimated from the time history of the cross-flow component of velocity at a point in the middle cell located at  $(x/D=4.9, y/D=1.5$ , and  $z/D=15.1$ ). The  $St_v$  is based on the time period of one cycle of

variation of  $v$ . Also shown in the same figure is the variation of the oblique shedding frequency estimated from the parallel shedding frequency and the oblique shedding angle [from Fig. 10(a)] via the relation:  $St_\theta = St_0 \cos \theta$ . The value of  $St_0 (=0.1343)$  has been obtained by computations for the  $Re=60$  flow with slip-wall end conditions that induce parallel shedding. Care has been taken to measure the angle of oblique vortices as close as possible to the point where  $St$  is reported. From Fig. 10(b), we note that the time variation of  $St_\theta$  matches quite well with that of  $St_v$ . Frames (c) and (e) of Fig. 6 show that the vortex dislocation is closest to the probe at  $t \sim 950$  and 1220 time units. At these time instants  $\theta$  is close to its maximum and  $St_\theta$  achieves a low value. Based on these observations we conclude the following for the  $Re=60$  flow. The boundary layer on the side walls promotes oblique shedding and vortex dislocations. The vortex dislocations lead to a low frequency modulation in all flow quantities including the angle of the vortices and the frequency itself. The frequency achieves a low and the oblique angle a large value as the dislocations pass the point of observation.

#### E. Time variation of fluctuations in velocity

Schumm *et al.*<sup>22</sup> using the Stuart–Landau equation, found a linear growth in the amplitude of fluctuating velocity in the wake of a circular cylinder for  $Re$  up to 60. Leweke and Provansal<sup>23</sup> showed, via modeling the flow by Ginzburg–Landau equation that the growth of the amplitude

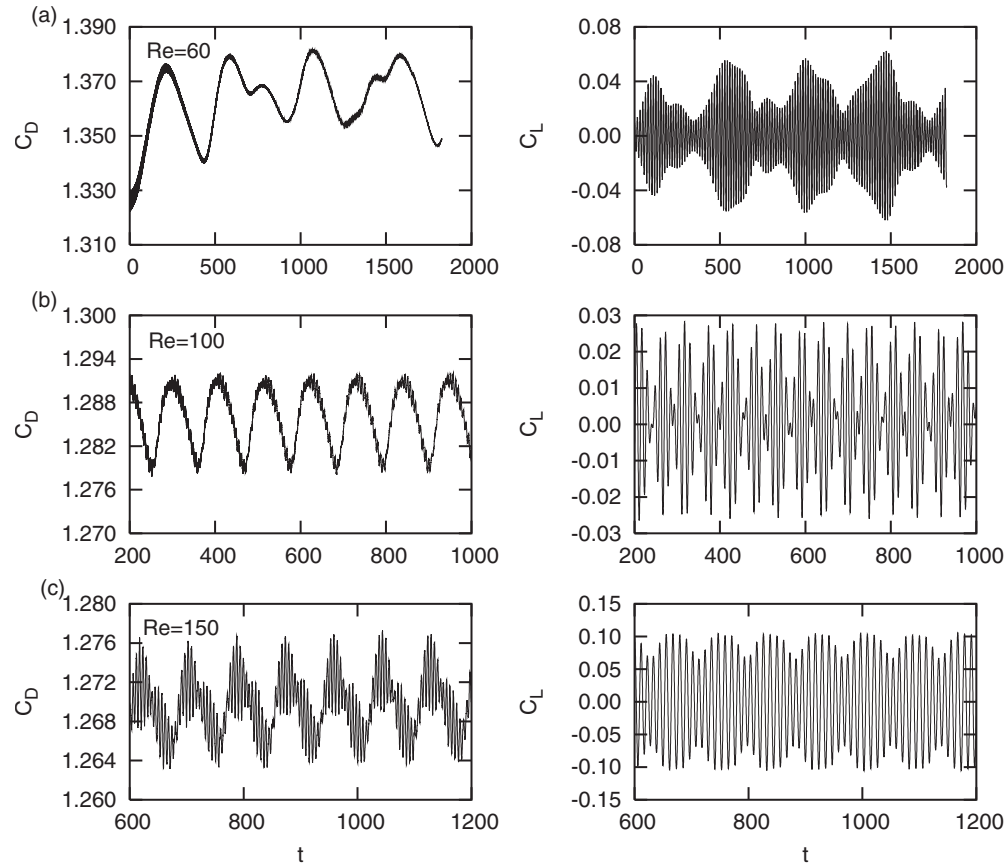


FIG. 12. Flow past a circular cylinder: time histories of the drag (left) and lift (right) coefficients at different  $Re$ . Oblique vortex shedding is promoted by the no-slip condition on velocity on one of the side walls.

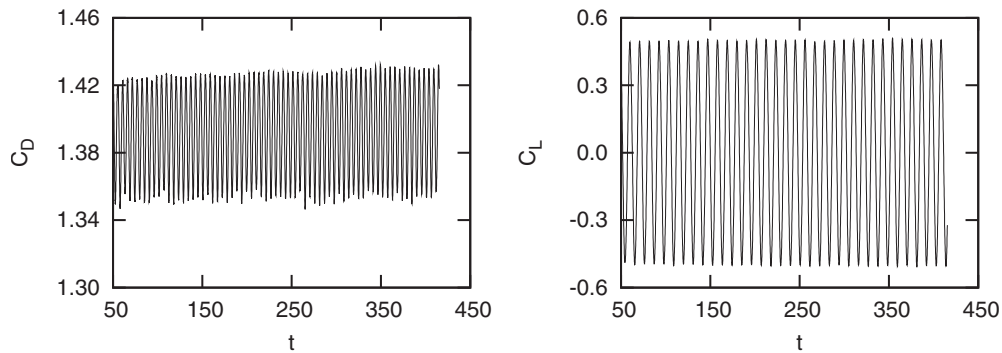


FIG. 13.  $Re=150$  flow past a circular cylinder with slip conditions on the side walls: time histories of the drag (left) and lift (right) coefficients. Parallel vortex shedding is observed in this case.

in the fluctuations of the streamwise velocity component increases with an increase in  $Re$ . The present computations confirm this trend. For the  $Re=60$  flow, the amplitude of fluctuations is found to vary with time. We further investigate, for this flow, the correlation between the amplitude of velocity fluctuations and the oblique angle of vortices. The velocity fluctuation is sampled at  $(x/D, y/D, z/D) = (4.5, 0.3, 24.8)$ . The Strouhal number is determined for each cycle of the velocity fluctuation. This is also utilized to estimate the angle of vortex shedding via the relation:  $St_\theta = St_0 \cos \theta$  as detailed in Sec. III D. Figure 11 shows the time variation of  $\cos \theta$  as well as the rms value of the streamwise component of velocity. The  $y$ -scale of the two signals are scaled appropriately to show, qualitatively, the phase between  $\cos \theta$  and  $u_{rms}$ . From the figure it is seen that the variation of  $u_{rms}$  is similar to that of  $\cos \theta$ . This implies that,

for the  $Re=60$  flow, the intensity of velocity fluctuations reduces with increase in the oblique shedding angle of the vortices.

#### F. Aerodynamic coefficients

Figure 12 shows the time histories of the drag and lift coefficients for various  $Re$ . As is seen in other quantities, low frequency modulation in the time variation of  $C_D$  and  $C_L$  is observed for all  $Re$ . The time histories of  $C_D$  and  $C_L$  for  $Re=150$  flow with slip conditions on the velocity on the side walls are shown in Fig. 13. Parallel shedding is observed in this case. The variation in  $C_D$  and  $C_L$  is periodic in time and devoid of the low frequency oscillations that are observed for the flow with no-slip condition on velocity on one of the side walls.

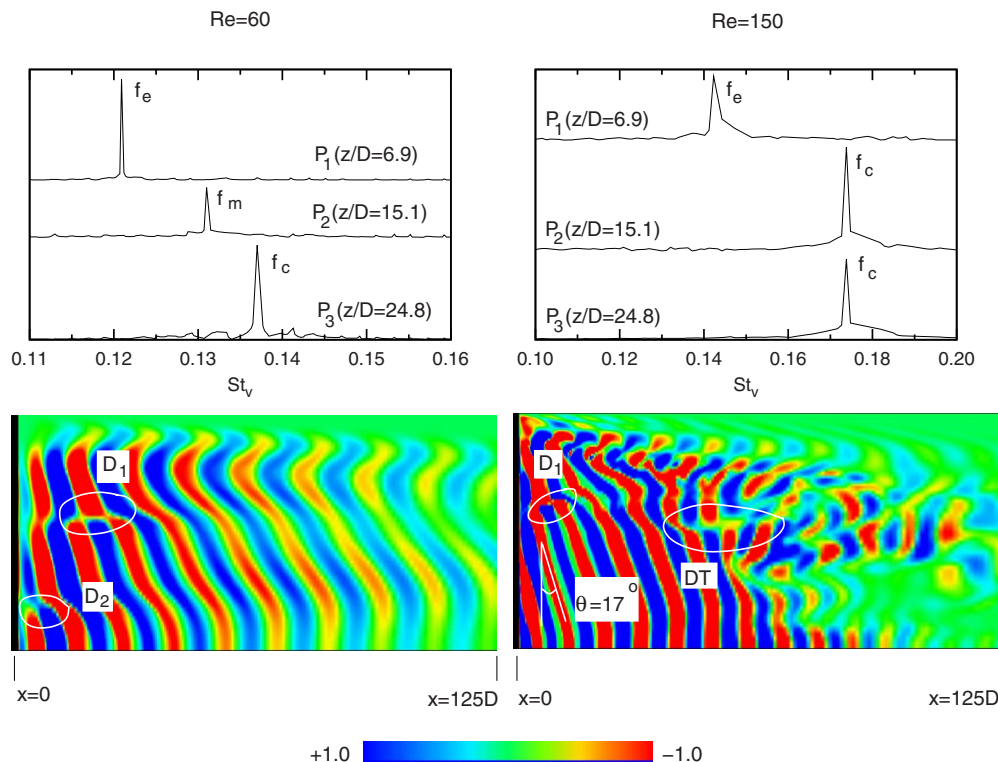


FIG. 14. (Color online)  $L_p=20D$  flow past a circular cylinder: power spectra of the cross-flow component of velocity,  $v$ , and instantaneous picture of spanwise vorticity on the  $xz$  plane passing through the axis of the cylinder at  $Re=60$  (left) and  $Re=150$  (right). The  $(x/D, y/D)$  location for all the three probes is  $(4.9, 0.3)$ .

TABLE II. Comparison of the Strouhal number corresponding to the shedding frequency of various cells for  $L_p=5D$  and  $20D$  at  $Re=60$  and  $150$ .

Re	60		150	
	$5D$	$20D$	$5D$	$20D$
$S_e$	0.1238	0.1221	0.1445	0.1423
$S_L$	0.1309	0.1297		
$S_U$	0.1345	0.1330	0.1770	0.1738

The time period of the low frequency modulation in the  $C_D$  variation is very close to the time between the appearance of two dislocations. For example, for the  $Re=100$  flow, the time period of a low frequency oscillation in  $C_D$  is  $\sim 107$  time units [Fig. 12(b)], while it is  $\sim 110$  time units (Fig. 7) for the appearance of consecutive dislocations. These numbers for the  $Re=150$  flow are 86 and 90, respectively. Low frequency oscillations in  $C_D$  has received some attention in the past. Najjar and Balachandar<sup>21</sup> reported modulation in  $C_D$  in the  $Re=250$  flow past a normal flat plate. They observed that when the roll-up process of Karman vortices is close to the plate the drag is higher. During this time the vortices posses stronger spanwise vorticity, which causes higher Reynolds stresses in the near wake. This is associated with the lower time- and span-averaged base pressure. The lower drag results from the delayed roll-up process of the vortices when they are weaker. The low frequency modulation in  $C_D$  is the result of periodic shifting between the shedding of stronger and weaker Karman vortices.

For the  $Re=100$  and  $150$  flow, we observe that the lowest value of  $C_D$  corresponds to the time instant when a new spotlike dislocation makes its appearance in the near wake. As the dislocation is connected away from the cylinder the drag increases and again decreases as a dislocation begins to form. For example, for the  $Re=150$  flow, a vortex dislocation is seen in the near wake at  $t=830$  and  $920$  in Fig. 7. At these time instants the drag achieves close to minimum value, which can be noticed in Fig. 12(c).

### G. Effect of $L_p$ on oblique shedding

The effect of  $L_p$  (please see Fig. 1) is investigated. An increase in  $L_p$  is expected to cause an increase in the boundary layer thickness on the side wall at the location where the flow approaches the cylinder. This, in turn, is expected to affect the angle of oblique vortex shedding. Computations are carried out for  $Re=60$  and  $150$  and results compared for two values of  $L_p$  ( $=5D$  and  $20D$ ). Figure 14 shows the power

spectra of the cross-flow component of velocity and an instantaneous picture of the vorticity field for  $L_p=20D$ . Qualitatively, the flow structure is same as the one observed for  $L_p=5D$ ; three cells for  $Re=60$  and two cells for the  $Re=150$  flow are formed along the span. The angle of oblique vortices changes with time for the  $Re=60$  flow for both values of  $L_p$ . For the  $Re=150$  flow, the oblique angle is  $\theta=17^\circ$  for  $L_p=20D$  as seen from Fig. 14. The corresponding angle, for  $L_p=5D$ , is  $12^\circ$ , as shown in Fig. 3. This study shows that the increase in the boundary layer thickness on the side wall leads to an increase in the oblique angle of vortices. This is discussed in more detail in Sec. III H in this paper. Table II shows the nondimensional shedding frequency in various cells for the computations. The values from  $L_p=5D$  and  $20D$  are quite close. The difference in the values for  $Re=150$  is consistent with the difference in the oblique angle of vortices obtained for the two values of  $L_p$ . By utilizing the relationship  $St_o=St_\theta/\cos \theta$ , the value of  $St_o$  for the central cell is estimated to be  $St_o=0.1817$  for  $L_p=20D$  and  $St_o=0.1809$  for  $L_p=5D$ . Both these values are in good agreement with  $St_o=0.1834$  reported by Williamson.<sup>5</sup>

### H. Variation of the shedding angle with the thickness of the boundary layer on side wall

The shedding angle of the vortices depends on several variables. These include  $Re$ ,  $L_p$ , and  $AR$ . The effect of  $Re$  is seen from Figs. 3 and 4(a). The effect of the aspect ratio of the cylinder on the shedding angle for  $Re=100$  flow is shown in Fig. 4. Similarly, the effect of  $L_p$  can be seen by comparing Figs. 3 and 14 for the  $Re=60$  and  $150$  flow. The factor that has the most significant effect on the angle of shedding appears to be the boundary layer thickness on the side wall. For a cylinder of given aspect ratio ( $AR=60$ ) we now explore the relationship between the two for the combined data for the various values of  $L_p$  and  $Re$  already presented. Listed in Table III is the shedding angle along with the normalized thickness of the boundary layer on the side wall,  $\delta/D$ , at the location of the cylinder for the various computations. The shedding angle varies in time for the  $Re=60$  flow. The data shown in the table is the average value. Figure 15 shows the variation of the shedding angle with the boundary for all the data shown in Table III. The linear best fit is also shown in the figure. A high positive correlation between  $\delta$  and  $\theta$  is observed from this figure. It appears that the angle of oblique vortices increases linearly with the thickness of boundary layer on the side wall.

TABLE III. Flow past a cylinder for two different values of  $L_p$ : variation of the angle of oblique vortices and the thickness of boundary layer on the side wall at the cylinder for various  $Re$ . The boundary layer thickness is estimated at the side wall for  $x/D=0$  and  $y/D=10$ .

$L_p$	Re=60		Re=100		Re=150	
	$\theta$	$\delta/D$	$\theta$	$\delta/D$	$\theta$	$\delta/D$
5D	$14^\circ$	1.362	$15^\circ$	1.077	$12^\circ$	0.883
20D	$25^\circ$	2.839			$17^\circ$	1.827

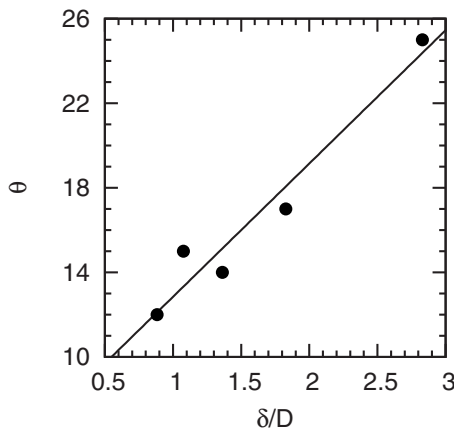


FIG. 15. Flow past a circular cylinder of  $AR=60$ : variation of the angle of oblique shedding with the normalized thickness of the boundary layer on the side wall. The boundary layer thickness is measured at  $x/D=0$  and  $y/D=10$ .

#### IV. CONCLUSIONS

Oblique shedding in the flow past a circular cylinder has been investigated numerically using a stabilized finite element method. No-slip condition on one of the sidewalls leads to the formation of a boundary layer which promotes oblique vortex shedding. Simulations have been carried out at  $Re=60$ , 100, and 150. In this regime the flow is devoid of the modes A and B type 3D instabilities. The aspect ratio of the cylinder considered is 60. Symmetry conditions are imposed at the mid span; only one half of the spanwise length is simulated.

At all the three  $Re$  the primary vortex shedding occurs in cells. Spotlike vortex dislocations form at the junction of the cells. At  $Re=60$ , three cells are observed along the span: end, middle, and central. The vortex shedding frequency increases from the end toward the central cell. The middle cell is more prominent than the central cell and dictates the overall primary frequency variation of the flow and the aerodynamic coefficients. The frequency of the appearance of the spotlike vortex dislocations, at the junction of the cells, is related to the difference in the vortex shedding frequency across the cells. The dislocations at the junction of end and middle cells appear more frequently than the ones between middle and central cells. The vortex shedding frequency in the cells is found to vary with time. The extent of variation of the frequency is found to increase with  $Re$ . Its variation is associated with a low frequency modulation that is accompanied with the appearance of dislocations. The dislocation appears at the time instant at which the frequency of vortex shedding is minimum. The angle of the oblique vortices in the middle cell also changes with the same temporal frequency. It is found that the vortex shedding frequency in the middle cell is related to the frequency observed for parallel shedding and the angle of the oblique vortices in the same way as has been proposed earlier for the case when the vortex shedding frequency and the oblique angle do not change with time ( $St_\theta = St_0 \cos \theta$ ). The time variation of the intensity of velocity fluctuations is also related to the unsteadiness in the angle of vortices; the intensity is found to vary as  $\cos \theta$ .

At  $Re=100$  and 150, only two cells are observed: end and central. The vortex shedding frequency as well as the oblique angle of the vortices in the central cell does not change with time for these  $Re$ . Very good agreement with the data from earlier studies is observed. The angle of the oblique vortices is seen to affect the velocity fluctuations in the flow. It is observed that the rms value of the velocity decreases with the increase in the angle of the oblique vortices. Computations have also been carried out for  $Re=100$  flow for a cylinder with larger aspect ratio,  $AR=120$ . It is found that the size of the end cell remains virtually the same but the oblique angle of the vortices depends on the aspect ratio of the cylinder.

The aerodynamic coefficients exhibit a low frequency modulation which is also found to be caused by the vortex dislocations. Lowest value of drag is achieved at a time instant corresponding to the appearance of a new dislocation in the near wake. The frequency of the dislocations and their impact on the amplitude of low frequency variations in the flow increases with  $Re$ . The effect of the length of the end plate on the flow is investigated. It is found that an increase in the length leads to an increase in the oblique angle of the vortices and a corresponding decrease in the vortex shedding frequency. Qualitatively, the flow remains the same. The shedding angle of the oblique vortices depend on several variables such as  $Re$ ,  $L_p$ , and  $AR$ . The  $Re$  and  $L_p$  directly affect the boundary layer thickness on the side wall. The dependence of the shedding angle for a cylinder of fixed aspect ratio on the height of the boundary layer on the side wall is explored. The oblique shedding angle, for various lengths of end plate and  $Re$ , is found to vary linearly with the thickness of the boundary layer on the side wall.

<sup>1</sup>C. H. K. Williamson, "Vortex dynamics in the cylinder wake," *Annu. Rev. Fluid Mech.* **28**, 477 (1996).

<sup>2</sup>B. Kumar and S. Mittal, "Prediction of critical Reynolds number for the flow past a circular cylinder," *Comput. Methods Appl. Mech. Eng.* **195**, 6046 (2006).

<sup>3</sup>E. Berger and R. Wille, "Periodic flow phenomena," *Annu. Rev. Fluid Mech.* **4**, 313 (1972).

<sup>4</sup>A. Slaouti and J. H. Gerrard, "An experimental investigation of the effects on the wake of a circular cylinder towed through the water at low Reynolds numbers," *J. Fluid Mech.* **112**, 297 (1981).

<sup>5</sup>C. H. K. Williamson, "Oblique and parallel modes of vortex shedding in the wake of a circular cylinder at low Reynolds numbers," *J. Fluid Mech.* **206**, 579 (1989).

<sup>6</sup>C. H. K. Williamson, "The natural and forced formation of spot-like 'vortex dislocations' in the transition of a wake," *J. Fluid Mech.* **243**, 393 (1992).

<sup>7</sup>P. Albarede and P. Monkewitz, "A model for the formation of oblique shedding and 'chevron' patterns in cylinder wakes," *Phys. Fluids A* **4**, 744 (1992).

<sup>8</sup>M. Hammache and M. Gharib, "An experimental study of the parallel and oblique vortex shedding from circular cylinders," *J. Fluid Mech.* **232**, 567 (1991).

<sup>9</sup>C. H. K. Williamson, "The existence of two stages in the transition to three-dimensionality of a cylinder wake," *Phys. Fluids* **31**, 3165 (1988).

<sup>10</sup>D. Gerich and H. Eckelmann, "Influence of end plates and free ends on the shedding frequency of circular cylinders," *J. Fluid Mech.* **122**, 109 (1982).

<sup>11</sup>M. Gaster, "Vortex shedding from slender cones at low Reynolds numbers," *J. Fluid Mech.* **38**, 565 (1969).

<sup>12</sup>H. Eisenlohr and H. Eckelmann, "Vortex splitting and its consequences in the vortex street wake of cylinders at low Reynolds numbers," *Phys. Fluids A* **1**, 189 (1989).

- <sup>13</sup>P. M. Yang, H. Mansy, and D. R. Williams, "Oblique and parallel wave interaction in the near wake of a circular cylinder," *Phys. Fluids A* **5**, 1657 (1993).
- <sup>14</sup>T. Leweke, M. Provansal, G. D. Miller, and C. H. K. Williamson, "Cell formation in cylinder wakes at low Reynolds numbers," *Phys. Rev. Lett.* **78**, 1259 (1997).
- <sup>15</sup>O. Inoue and A. Saukuragi, "Vortex shedding from a circular cylinder of finite length at low Reynolds numbers," *Phys. Fluids* **20**, 033601 (2008).
- <sup>16</sup>S. Mittal, "Computation of three-dimensional flows past circular cylinder of low aspect ratio," *Phys. Fluids* **13**, 177 (2001).
- <sup>17</sup>Y. Saad and M. Schultz, "GMRES: A generalized minimal residual algorithm for solving nonsymmetric linear systems," *SIAM J. Sci. Comput. (USA)* **7**, 856 (1986).
- <sup>18</sup>T. K. Prasanth and S. Mittal, "Vortex-induced vibrations of a circular cylinder at low Reynolds numbers," *J. Fluid Mech.* **594**, 463 (2008).
- <sup>19</sup>H. Zhang, U. Fey, B. R. Noack, M. Konig, and H. Eckelmann, "On the transition of the cylinder wake," *Phys. Fluids* **7**, 779 (1995).
- <sup>20</sup>O. Inoue and Y. Suzuki, "Beat of sound generated by flow past three side-by-side square cylinders," *Phys. Fluids* **19**, 048102 (2007).
- <sup>21</sup>F. M. Najjar and S. Balachandar, "Low-frequency unsteadiness in the wake of a normal flat plate," *J. Fluid Mech.* **370**, 101 (1998).
- <sup>22</sup>M. Schumm, E. Berger, and P. A. Monkewitz, "Self-excited oscillations in the wake of two-dimensional bluff bodies and their control," *J. Fluid Mech.* **271**, 17 (1994).
- <sup>23</sup>T. Leweke and M. Provansal, "The flow behind rings: Bluff body wakes without end effects," *J. Fluid Mech.* **288**, 265 (1995).